Nano Research
2020, 13(7): 1867–1874
ISSN 1998-0124 CN 11-5974/O4
https://doi.org/10.1007/s12274-019-2547-9

Research Article

Superior wide-temperature lithium storage in a porous cobalt vanadate

Haoliang Chen[1], Dan Yang[1], Xueye Zhuang[1], Dong Chen[1], Weiling Liu[2], Qi Zhang[1], Huey Hoon Hng[2], Xianhong Rui[1,3] (✉), Qingyu Yan[2] (✉), and Shaoming Huang[1] (✉)

[1] *Guangzhou Key Laboratory of Low-Dimensional Materials and Energy Storage Devices, Collaborative Innovation Center of Advanced Energy Materials, School of Materials and Energy, Guangdong University of Technology, Guangzhou 510006, China*
[2] *School of Materials Science and Engineering, Nanyang Technological University, Singapore 639798, Singapore*
[3] *State Key Laboratory of Vanadium and Titanium Resources Comprehensive Utilization, Panzhihua 617000, China*

Received: 10 September 2019 / **Revised:** 10 October 2019 / **Accepted:** 16 October 2019

ABSTRACT

Lithium ion batteries (LIBs) that can be operated under extended temperature range hold significant application potentials. Here in this work, we successfully synthesized $Co_2V_2O_7$ electrode with rich porosity from a facile hydrothermal and combustion process. When applied as anode for LIBs, the electrode displayed excellent stability and rate performance in a wide range of temperatures. Remarkably, a stable capacity of 206 mAh·g^{-1} was retained after cycling at a high current density of 10 A·g^{-1} for 6,000 cycles at room temperature (25 °C). And even when tested under extreme conditions, i.e., –20 and 60 °C, the battery still maintained its remarkable stability and rate capability. For example, at –20 °C, a capacity of 633 mAh·g^{-1} was retained after 50 cycles at 0.1 A·g^{-1}; and even after cycling at 60 °C at 10 A·g^{-1} for 1,000 cycles, a reversible capacity of 885 mAh·g^{-1} can be achieved. We believe the development of such electrode material will facilitate progress of the next-generation LIBs with wide operating windows.

KEYWORDS

lithium-ion battery, anode material, cobalt vanadate, porous structure, wide-temperature performance

1 Introduction

In recent years, lithium ion batteries (LIBs) are dominating market in consumer electronics with steady improvement in both energy and power density. To power an electric vehicle (EV) or a hybrid EV, not only a high energy density but also a stable charge/discharge cycling over a wide temperature range (e.g., –20 °C ≤ T ≤ 60 °C) is required [1–8]. However, at elevated temperatures, self-discharging reaction between the electrolyte and electrode is accelerated, resulting in rapid capacity fading and short cycle life of batteries [9]. Besides, some safety issues emerge with the increased temperature, e.g., thermal runaway, dangerous electrode-solution interactions, and etc. [10–15]. On the other hand, both energy and power density of LIBs are substantially reduced as the temperature falls below 0 °C, which mainly arises from the reduced ionic conductivity of electrolyte and limited diffusivity of lithium ions in electrodes at low temperatures [16–21]. To satisfy high-power applications with variable operation temperatures, it is critical to improve both low and high temperature performance of current LIBs with minimal capacity fading, where stable anode materials with high capacity and optimized structure hold a key role.

Recently, transition metal vanadates (TMVs) are attracting extensive attention as anodes for LIBs [22–27]. In particular, $Co_2V_2O_7$, one typical vanadate with mixed-valence cations in one single crystal structure, are regarded as a promising anode material [28–30]. Its intriguing electrochemical reactivity mainly comes from the complex chemical composition, interfacial effects and synergistic benefits endowed by different metal species [31–34]. At the meantime, with combined conversion and insertion mechanism from the synergetic presence of both vanadium and cobalt elements, a much higher specific capacity of ~ 1,000 mAh·g^{-1} can be achieved, i.e., typical $Co_2V_2O_7$ anode can take up reversibly to ~ 12.4 Li ions per formula unit in the voltage range of 0.01–2.5 V during the charge/discharge process [33]. However, up to now, the electrochemical capacity attenuation of the $Co_2V_2O_7$, especially at high current density and non-ambient temperatures, is still a noticeable problem on account of sluggish Li^+ diffusion kinetics and the large volume change of electrode during cycling.

Downsizing the electrode material with tailored nanostructures has proved to be efficient strategy in mitigating the structural stress and bringing about improved electrochemical performance [35–40]. For example, Wu et al. reported a water bath method for synthesis of hexagonal nanoplatelets of $Co_2V_2O_7$, which exhibited a reversible capacity as high as 866 mAh·g^{-1} (current density: 500 mA·g^{-1}) with 100% capacity retention after 150 cycles [30]. Hierarchical $Co_2V_2O_7$ nanosheets consisted of interconnected nanoparticles were synthesized by Luo et al., and a reversible capacity of 441 mAh·g^{-1} at 5.0 A·g^{-1} after 900 cycles was achieved [33]. Despite of the marvelous application potential, so far the cycling and rate performance of nano-/micro-$Co_2V_2O_7$ particles are still inferior to many other metal oxides. Moreover, hardly any report has dealt with performance of $Co_2V_2O_7$ under variable temperatures, which actually is more important in terms of practical applications.

Address correspondence to Xianhong Rui, xhrui@gdut.edu.cn; Qingyu Yan, alexyan@ntu.edu.sg; Shaoming Huang, smhuang@gdut.edu.cn

Here in this work, we have successfully synthesized porous $Co_2V_2O_7$ hexagonal prisms (denoted as P-CVO-HPs) anode material with hydrothermal followed by a combustion process. Featured with the porous structure, the electrode showed excellent electrochemical performance, e.g., a stable and high specific capacity of 754 mAh·g^{-1} after 1,000 cycles at 5 A·g^{-1}, good long-term cyclability (206 mAh·g^{-1} after 6,000 cycles at 10 A·g^{-1}) and excellent rate performance were achieved. More significantly, the electrodes demonstrated remarkable response over a wide range of operating temperatures. Even operated under extreme conditions (−20 to 60 °C), the battery still maintained excellent cycling stability and rate capability (e.g., a capacity of 633 mAh·g^{-1} was achieved when operated at 0.1 A·g^{-1} under −20 °C for 50 cycles; after cycling under 60 °C at 10 A·g^{-1} for 1,000 cycles, a capacity of 885 mAh·g^{-1} was retained).

2 Experimental

2.1 Synthesis of P-CVO-HPs

All the chemicals were analysis grade and used without further purification. To start a typical procedure to synthesize porous $Co_2V_2O_7$ hexagonal prisms (P-CVO-HPs), 1.0 mmol NH_4VO_3 was initially dissolved into 35 mL deionized water at 80 °C under vigorous stirring. Then, certain amount (1.0 mmol) of LiOH was added to the above solution, which became transparent and colorless after several minutes. Subsequently, 1.5 mmol $CoCl_2·6H_2O$ was added and brown suspension was formed. After stirring for 10 min, the brown suspension was transferred into a 50 mL Teflon-lined autoclave and kept at 180 °C for 12 h. After cooling to room temperature in air, the as-prepared precursor was collected and washed with distilled water and ethanol several times by centrifugation and then dried by lyophilizing for 48 h. To obtain porous structure, the as-prepared precursor was calcined in air at 450 °C for 2 h with the heating rate of 5 °C·min^{-1}.

2.2 Material characterization

The composition and phase purity of the as-prepared samples were analyzed by powder X-ray diffraction (XRD, Rigaku D-Max 2200, Cu-Kα radiation: λ =1.5406 Å) with 2θ ranged from 10° to 80°. The morphology and detailed nanostructure of the products were characterized by field-emission scanning electron microscopy (FESEM, Hitachi SU-8220), and transmission electron microscopy (TEM, FEI Tecnail F30) which is equipped with an energy-dispersive spectroscopy (EDS) detector and selected area electron diffraction (SAED). The valences of elements in the product were investigated by X-ray photoelectron spectroscopy (XPS, Escalab 250Xi).

2.3 Electrochemical investigation

The electrochemical performances of the sample were tested through assembling the sample into 2032-type coin cells, which were operated in an argon-filled dry glove box. The slurry, which was composed of 70% active material (i.e., P-CVO-HPs), 20% carbon nanotubes (CNTs) and 10% polyvinylidene fluoride (PVDF) in N-methyl-2-pyrrolidone (NMP) solvent, was drop-casted on a copper foil and dried in the vacuum oven at 80 °C for 12 h, and then punched into disks (Φ = 15 mm) to fabricate the working electrode. Later, the working electrode was paired with clean lithium foil as the counter electrode, Celgard 2400 membrane as the separator and 1 M $LiPF_6$ in ethylene carbonate (EC)-dimethyl carbonate (DMC) (1:1, v/v) as electrolyte, to achieve a 2032-type coin cell. The galvanostatic discharge and charge states of coin cells were tested on a Neware battery test system within the voltage range of 0.01–3.0 V vs. Li/Li$^+$. Cyclic voltammetry (CV) measurement was carried out on electrochemical station (CHI 660C) at different scanning rates from 0.1 to 1.0 mV·s^{-1} and the electrochemical impedance spectra (EIS) were recorded with a frequency range of 0.01–10^5 Hz.

3 Results and discussion

The synthesis process of P-CVO-HPs is illustrated in Fig. S1 in the Electronic Supplementary Material (ESM). Typically, a hydrothermal process was carried out to form the precursor of hydrated $Co_2V_2O_7$ (Fig. S2 in the ESM), followed by an annealing process (450 °C for 2 h in air) to remove crystal water and generate rich porosity. The crystallographic structure and phase purity of the final product was determined by powder X-ray diffraction (XRD). As shown in Fig. 1(a), all the intense diffraction peaks can be well indexed to the monoclinic $Co_2V_2O_7$ (JCPDS No. 70-1189) with no impurity phase detected. To further identify the surface chemical information of the P-CVO-HPs, X-ray-photoelectron-spectroscopy (XPS) analysis was carried out and the results are shown in Figs. 1(b)–1(e). From the wide-scan survey spectrum of P-CVO-HPs, coexistence of the Co 2p, V 2p and O 1s regions can be clearly identified. The

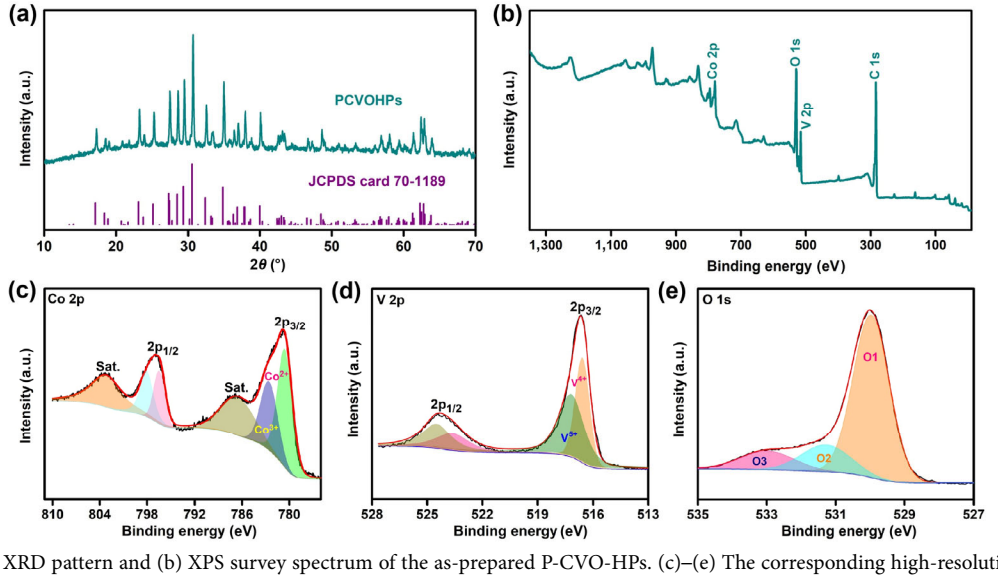

Figure 1 (a) The XRD pattern and (b) XPS survey spectrum of the as-prepared P-CVO-HPs. (c)–(e) The corresponding high-resolution XPS spectra of Co 2p, V 2p and O 1s peaks.

Co 2p spectrum is typically located at 797.2 (Co $2p_{1/2}$) and 781.1 eV (Co $2p_{2/3}$), accompanied by two shakeup satellite peaks (786.4 and 802.3 eV), which are characteristic of Co^{2+} [30]. Further refined fitting revealed that Co^{3+} is also presented, which may be attributed to partial oxidation from combustion in air. Four peaks appeared in the V 2p spectrum and the results are shown in Fig. 1(d). Among them, two peaks of V 2p at the binding energies of 517.5 (V $2p_{3/2}$) and 524.9 eV (V $2p_{1/2}$), accompanied by a spin–orbit splitting of 7.4 eV, are assigned to V^{5+} [37]. The peaks emerged at 516.7 and 523.8 eV are assigned to presence of V^{4+} [41]. These results indicate that Co^{2+}, Co^{3+}, V^{4+}, and V^{5+} co-exist on the surface of the products. The O 1s spectrum can be fitted into three peaks denoted as O1, O2 and O3, locating at 529.9 (O1), 531.3 (O2), and 533.0 eV (O3) (Fig. 1(e)), which are ascribed to the M–O, –OH, and C=O, respectively [42].

Field emission scanning electron microscopy (FESEM) was used to check morphology of the product. The panoramic and magnified FESEM images (Figs. 2(a)–2(c)) show that the as-prepared product is composed of uniform hexagonal prisms with heights of 1.5 μm and widths of around 500 nm. Moreover, the high-magnification FESEM image (Fig. 2(c)) reveals that the sintering procedure has endowed the hexagonal prisms rough. In particular, presence of large amount of bright light spots in the TEM image (Fig. 2(d)) suggests the hexagonal prisms had transformed from solid into porous structure upon the annealing process. Mercury porosimetry further confirmed the porous nature of the product, and the average pore diameter is determined to be ~ 400 nm (Fig. S3 in the ESM). Two sets of lattice spacing are observed from high-resolution TEM (HRTEM) (Fig. 2(e)), that are, 0.25 and 0.29 nm, which correspond to the crystal planes of (113) and ($\bar{2}02$) of monoclinic $Co_2V_2O_7$, respectively. The selected area electron diffraction (SAED) pattern (Fig. 2(f)) describes well-defined diffraction spots with hexagonal symmetry, indicating good crystallinity of the products, which is consistent with the XRD result as well. Moreover, electron dispersive spectroscopy (EDS) results show that the hexagonal prisms are mainly composed of the elements of Co, V and O, which are homogeneously distributed in the prisms as revealed in the mapping images (Fig. 2(g)).

To better understand the growth process and precisely manipulate micro-structure of the final product, parameters involved in the reaction system were systematically investigated. As seen from Fig. 3(a) and Fig. S4(a) in the ESM, the pre-reaction suspension consists of many fine nanoparticles (~ 10 nm). After hydrothermal reaction for 2 h, these nanoparticles are self-organized into pillars with lengths of ~ 200 nm (Fig. 3(b) and Fig. S4(b) in the ESM). Continuous reaction (4 to 12 h) results in the gradual crystallization of hydrated CVO precursors (Fig. 3(c), and Figs. S2, S4(c)–S4(f) in the ESM), and subsequent annealing converts them into P-CVO-HPs (Fig. 3(d)). The whole process of the formation of P-CVO-HPs is thus schematically illustrated in Fig. 3(e). On the other hand, it has been found that the phase purity and hexagonal prism morphology were highly dependent on the amount of LiOH added in the solution. As shown in Fig. S5 in the ESM, pure hydrated $Co_2V_2O_7$ can be formed only when the dosage of LiOH was ranged between 0.75–1.25 mmol. Once lower than 0.5 mmol, a diffraction peak located at 22.4° was observed, which corresponds to the (022) planes of the impurity phase $CoV_2O_6{\cdot}2H_2O$ (JCPDS No. 80-0247). However, when the amount of LiOH was increased to more than 1.5 mmol, another impurity phase of CoV_3O_8 (JCPDS No. 89-7017) was detected. Variation in the LiOH dosages also brought about morphology transformation of the products. For instance, as the amount of LiOH increased from 0.3 to 0.75 mmol, morphology of the end products has changed from nanorods and irregular prisms into nanobelts and hexagonal prisms (Figs. S6(a)–S6(c) in the ESM). When the amount of LiOH was ranged between 1.25–1.75 mmol, irregular particles formed instead of the hexagonal prisms, with very few pencil-like structures presented (Figs. S6(d)–S6(f) in the ESM). Further increase of the LiOH to 2.0 mmol would result in the formation of "micro-bullets" with 15 μm in lengths (Fig. S6(g) in the ESM). In general, the ideal amount of LiOH should be around 1.0 mmol to generate uniform hexagonal prisms.

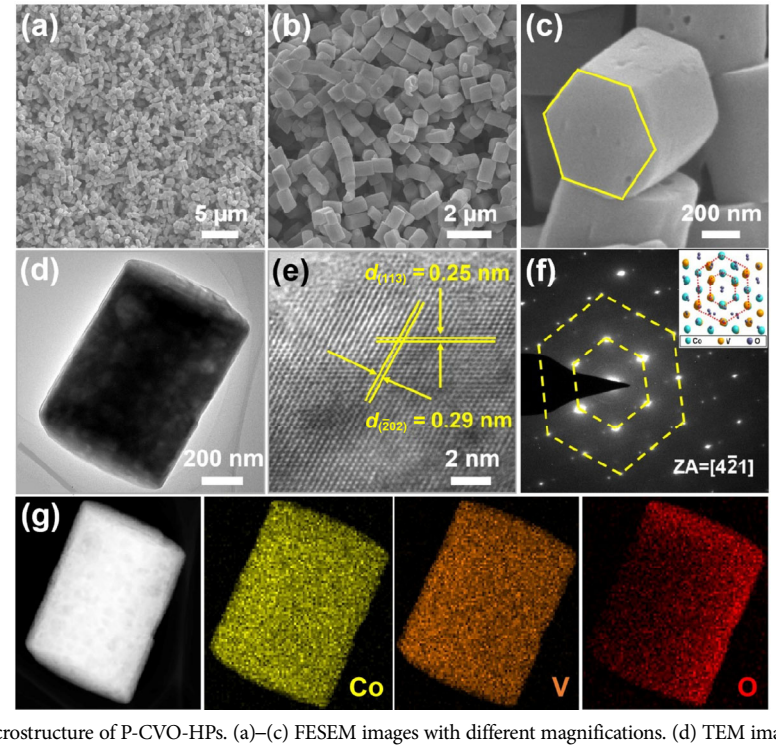

Figure 2 Morphology and microstructure of P-CVO-HPs. (a)–(c) FESEM images with different magnifications. (d) TEM image, (e) HRTEM image, (f) SAED pattern, and (g) STEM and the corresponding elemental mapping images indicating the homogeneous distribution of all three elements of Co, V and O.

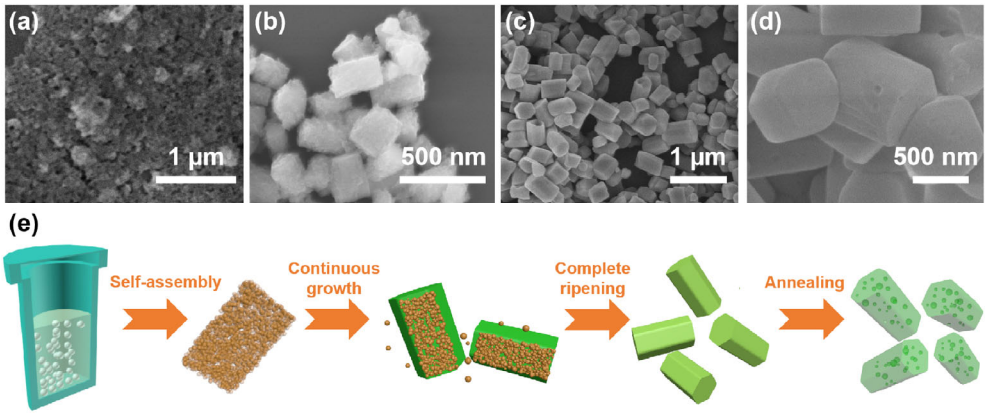

Figure 3 The formation process of the P-CVO-HPs. FESEM images of the pre-reaction suspension (a), hydrothermal intermediates ((b) 2 h and (c) 10 h), and final product (d). (e) Schematic diagram illustrating the growth process.

To evaluate the electrochemical performance of as-synthesized P-CVO-HPs, CR-2032 coin-type half-cells were assembled by using metallic lithium as the counter electrode and initially measured at room temperature (25 °C). The cyclic voltammogram (CV) profiles measured at a scan rate of 0.1 mV·s^{-1} within the voltage window of 0.01–3.0 V are shown in Fig. S7 in the ESM. The electrochemical behavior in the first cycle is a little distinctive from the subsequent cycles, which may be attributed to the irreversible formation of solid electrolyte interphase (SEI) film and the decomposition of the electrolyte. In particular, the intense peak at 0.62 V is attributed to the formation of CoO and $Li_xV_2O_5$, and the peak located at 0.16 V is assigned to the further reduction of CoO into metallic Co^0 matrix and the formation of SEI film. From the second cycle onward, repeated occurrence of the reduction peaks, located at 0.55 and 1.90 V, with their corresponding oxidation peaks at 1.34 and 2.40 V, are observed, indicative of a reversible Li^+ insertion/extraction process [31, 43]. The galvanostatic charge-discharge voltage profiles at a low current density of 100 mA·g^{-1} are displayed in Fig. 4(a). The voltage plateaus are consistent well with CV behaviors. During the first cycle, discharge and charge capacities of 2,163 and 1,472 mAh·g^{-1} are achieved (the initial Coulombic efficiency: 68%). Subsequent Li^+ uptake/removal are highly reversible, showing almost constant capacity at around 1,230 mAh·g^{-1} during 50 cycles (Fig. 4(b)).

High rate performance and stable cycling capability are the

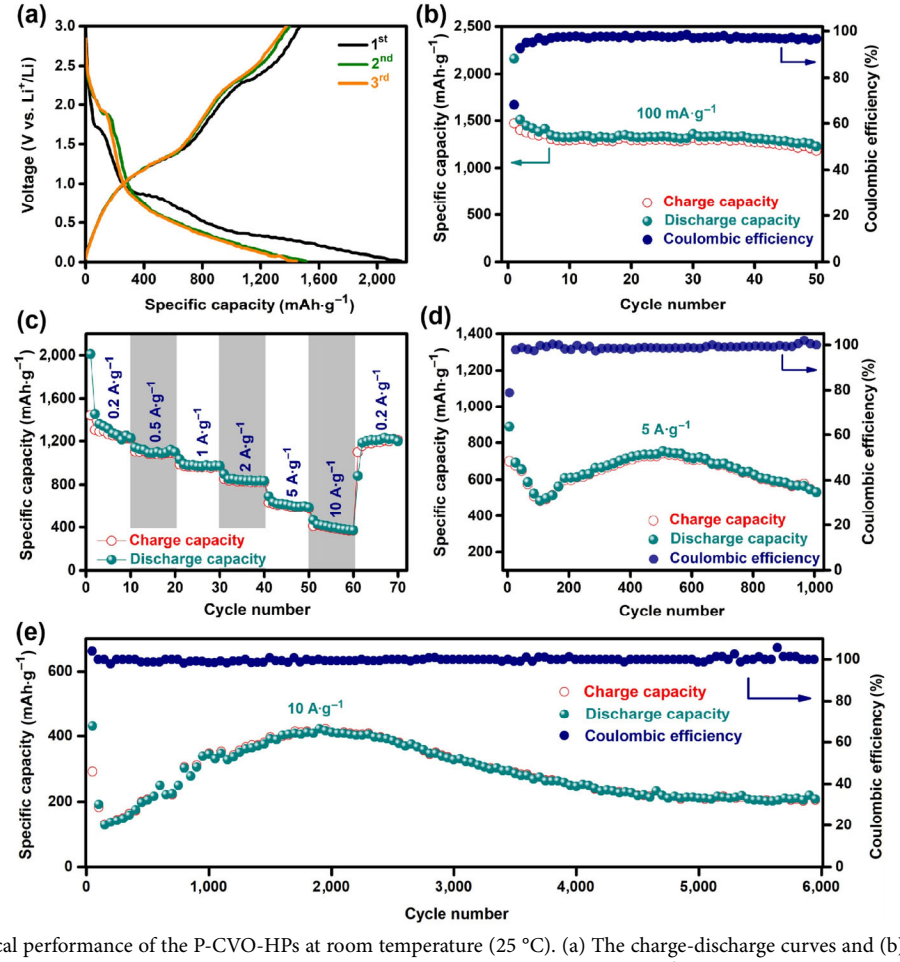

Figure 4 Electrochemical performance of the P-CVO-HPs at room temperature (25 °C). (a) The charge-discharge curves and (b) cycling performance at 100 mA·g^{-1}, (c) rate capability, and ((d) and (e)) long-term cycling stability at high rates of 5 and 10 A·g^{-1}, respectively.

main factors deciding the performance of electrode in practical applications. Therefore, the rate capability of the P-CVO-HPs with different current densities in ambient temperature was tested and the results are shown in Fig. 4(c). The battery delivers average capacities of 1,228, 1,099, 974, 836, 590 and 372 mAh·g^{-1} at current densities of 0.2, 0.5, 1, 2, 5 and 10 A·g^{-1}, respectively. Notably, after cycling at the various current densities, the specific capacity of 1,209 mAh·g^{-1} can be recovered when the current density is lowered to 0.2 A·g^{-1}, indicating good reversibility of the electrodes. Besides, the electrode also demonstrates excellent stability, even at high current densities. For example, after cycling at 5 A·g^{-1} for 1,000 cycles, the capacity of 532 mAh·g^{-1} is still reached with the Coulombic efficiency of close to 100% (from the 2nd cycle) during the whole cycling process (Fig. 4(d)). The long-term stability of the electrode is also remarkable at an ultrahigh current density of 10 A·g^{-1}, which delivers a stable capacity of 206 mAh·g^{-1} after 6,000 cycles (Fig. 4(e)). Notably, the capacity is suddenly decreased during the first several cycles and then recovered during the following cycles. It is because that the conversion reactions (i.e., the deconstruction of the crystal $Co_2V_2O_7$) generated volume expansion and the formation of solid electrolyte interface (SEI) layer would reduce the lithium storage capacity at early stage, and continuous charging and discharging can gradually activate the electrode and improve interfacial lithium storage ability [31, 32, 44].

To reveal the electrochemical mechanism of the P-CVO-HPs electrode, *ex-situ* XRD patterns under different charge and discharge state were investigated. As shown in Fig. 5(a), a structural phase transition can be clearly detected as the electrode was discharged to 0.6 V, where the peaks correspond to the CVO disappeared. Even when the electrode is charged back to 3 V, these CVO peaks are not recovered, indicating irreversibility of such phase transition. At the meantime, peaks corresponding to $Li_xV_2O_5$ are emerged when discharged to 0.2 V, of which the intensity increases with the charging process. Peaks related with formation of Li_2O are found when the electrode was fully discharged, and when the electrode was discharged to 2.4 V, the peak vanishes again. This indicates the reversibility of the formation and decomposition of Li_2O. Also, LiOH is detected from the intermediates, which might be originated from the reaction of Li_2O with water in exposed air. In contrary to the analysis from the CV curves, it is hard to identify peaks of Co and CoO from the *ex-situ* XRD patterns, which is likely due to formation of small size of metallic Co and their overlapped signal with the Cu substrate. For a more straightforward and intuitive understanding of the electrochemical process, STEM, HRTEM and mapping results during the fully discharged and charged state were collected. As shown in Figs. 5(b) and 5(e), accompanied with the insertion and de-insertion of Li ions, small nanoparticles appear and disappear around the hexagonal prisms. The HRTEM image (Fig. 5(c)) of an individual lithiated nanoparticle displays a crystal lattice with a spacing of 0.204 nm, corresponding to the (002) plane of Co (JCPDS No. 89-7094). The lattice fringe obtained from Fig. 5(f) is 0.245 nm, which corresponds to the (101) plane of CoO (JCPDS No. 89-2803), which suggests that the metallic Co is oxidized into CoO during the delithiation process. As can be clearly identified from the mapping results (Figs. 5(d) and 5(g)), elements of Co, V and O evenly distribute in the electrode at both fully charged and discharged states.

Based on the above analysis, the overall reaction mechanism can be summarized as below:

$$Co_2V_2O_7 + xLi^+ + xe^- \rightarrow 2CoO + Li_xV_2O_5 \quad (1)$$

$$CoO + Li_xV_2O_5 + (y+2)Li^+ + (y+2)e^- \leftrightarrow Co^0 + Li_2O + Li_{x+y}V_2O_5 \quad (2)$$

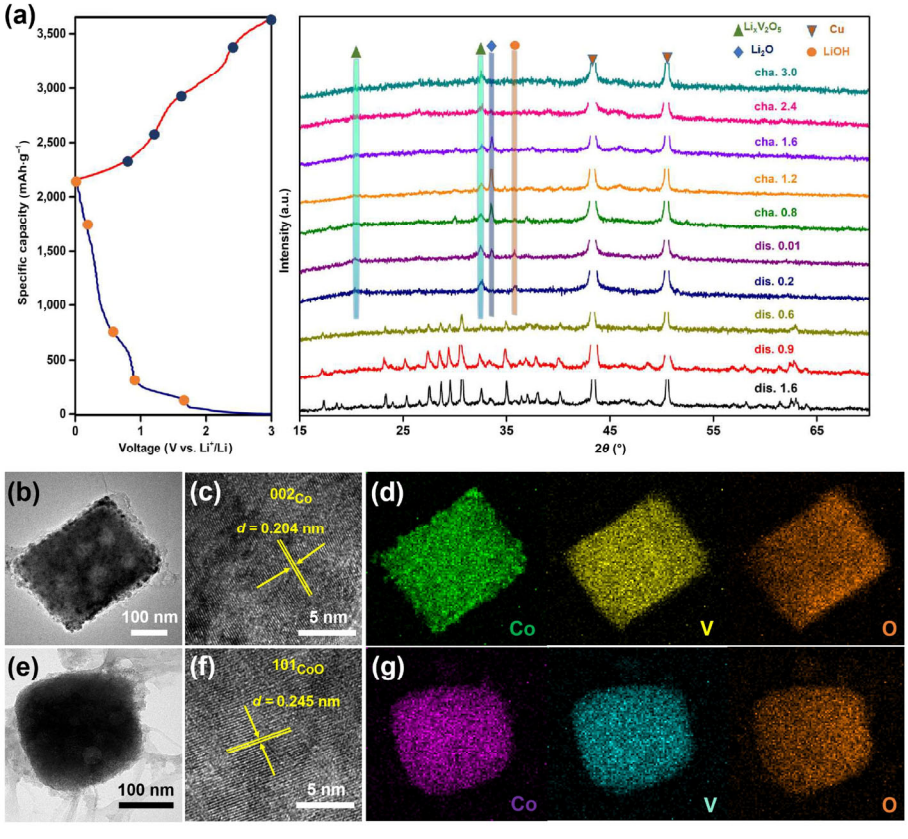

Figure 5 (a) *Ex-situ* XRD patterns of the P-CVO-HPs electrode measured at various discharge/charge states. ((b) and (e)) TEM images, ((c) and (f)) HRTEM images and ((d) and (g)) the corresponding EDS mapping images of the electrode observed at fully discharged ((b)–(d)) and charged ((e)–(g)) states.

To meet requirements of practical applications, a battery that can be operated at extreme conditions, e.g., temperature ranged from −20 to 60 °C, would be quite promising. Given the remarkable electrochemical performance manifested by the P-CVO-HPs at room temperature, we further tested their response under some tough conditions. At low temperature (−20 °C), the discharge-charge profiles at 100 mA·g^{-1} are similar to those at 25 °C, implying negligible polarization (Fig. 6(a)), and as a result, the electrode can still deliver high initial discharge and charge capacities of 1,094 and 627 mAh·g^{-1} respectively, and reversible 633 mAh·g^{-1} even after 50 cycles (Fig. 6(b)). At high temperature (60 °C), average capacities of 1,564, 1,466, 1,337, 1,195, 1,015 and 825 mAh·g^{-1} are achieved at current densities of 0.2, 0.5, 1, 2, 5 and 10 A·g^{-1}, respectively (Fig. 6(c) and Fig. S8 in the ESM). In addition, even when operated at 60 °C at 10 A·g^{-1} for 1,000 cycles, it still delivers a reversible capacity of 885 mAh·g^{-1} corresponding to 91% of the initial capacity (Fig. 6(d)). As compared to previously reported vanadate-based and metal oxide anodes (Table S1 in the ESM), our P-CVO-HPs anode demonstrates a more remarkable performance in terms of its high capacity, cycling stability and rate capability [43, 45–50].

To further understand the excellent performances, especially *the remarkable rate capability at high temperatures, the electro*-chemical kinetics of P-CVO-HPs electrode were investigated (Fig. 7). For analysis, CV curves of P-CVO-HPs operated at both ambient temperature and 60 °C with the scan rates ranged from 0.1 to 1.0 mV·s^{-1} were collected (Figs. 7(a) and 7(d)). Both anodic and cathodic peaks slightly shift with the variation of the scan rates, which resembles characteristic feature of the pseudo-capacitive material. As well-documented in earlier reports, the capacitive contribution can be analyzed by fitting the current (i) into a power law relationship with the sweep rate ($i = av^b$), where a is a constant, v is the sweep rate and b

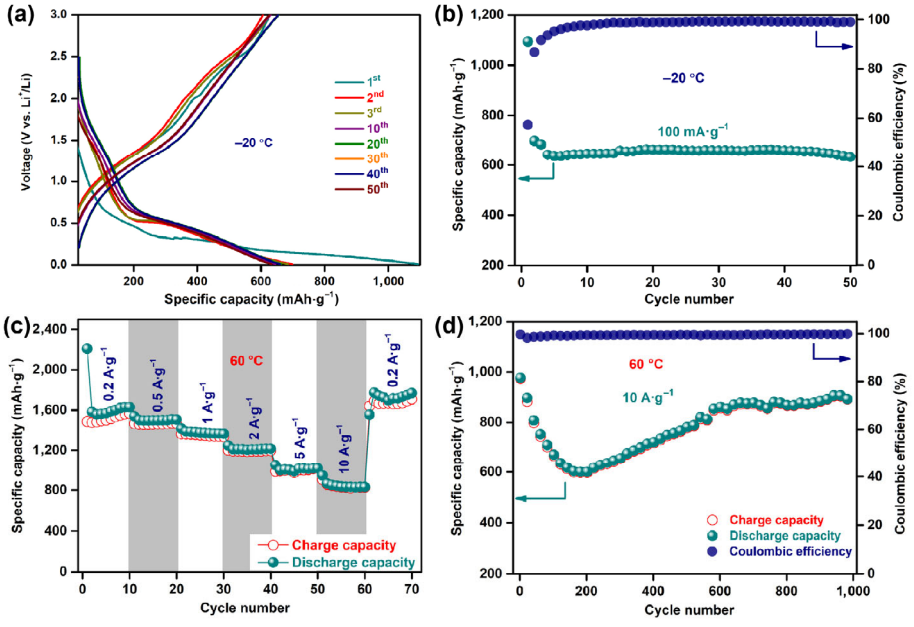

Figure 6 Electrochemical performance of the P-CVO-HPs at −20 and 60 °C. (a) The charge/discharge curves and (b) cycling performance (current density: 100 mA·g^{-1}) at −20 °C. (c) Rate capability and (d) high-rate (10 A·g^{-1}) cycling stability at 60 °C.

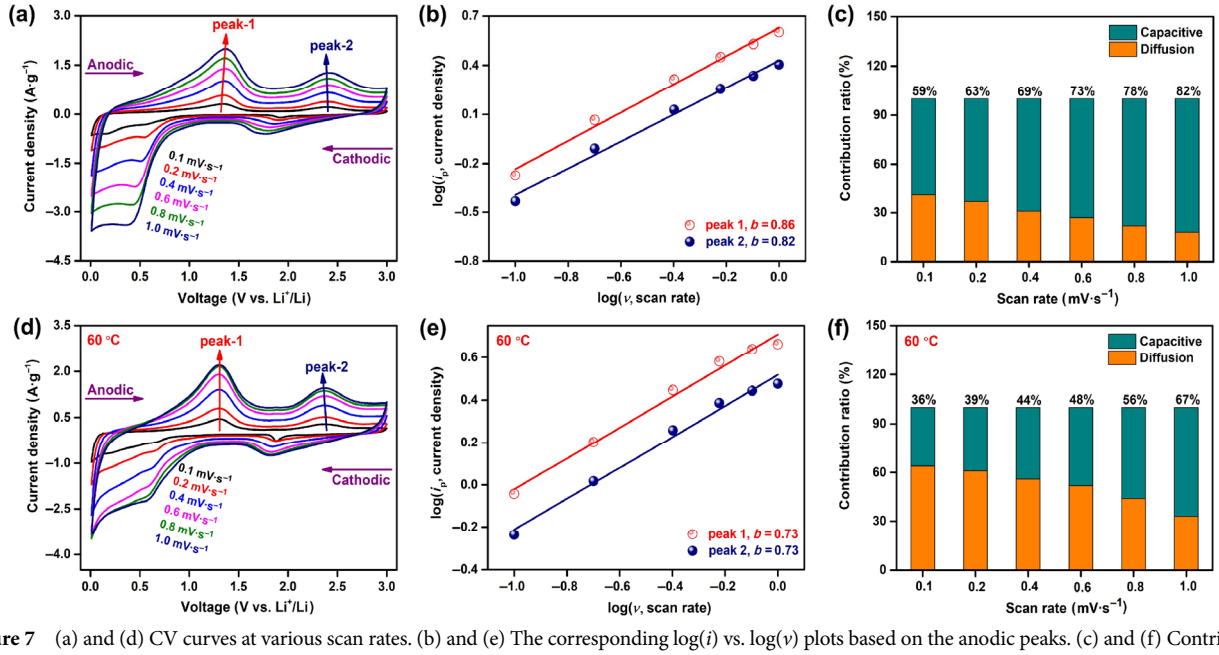

Figure 7 (a) and (d) CV curves at various scan rates. (b) and (e) The corresponding log(i) vs. log(v) plots based on the anodic peaks. (c) and (f) Contribution ratios of capacitive and diffusion effects at room temperature (25 °C) ((a)–(c)) and 60 °C ((d)–(f)).

is an estimate of the charge storage in the material. If b is 0.5, the current is diffusion-controlled and if b is 1, the current is capacitive [51]. Here, the b values are ranged between 0.5–1 in the CV curves at different operating temperatures (Figs. 7(b) and 7(e)) and the b value slightly decreased at 60 °C, suggesting more favored diffusion kinetics of the electrode at elevated temperatures. Furthermore, the diffusion and capacitive contribution could be more accurately determined by the equation $i(V) = k_1v + k_2v^{1/2}$, where k_1 and k_2 represent the capacitive and diffusion contribution to the current. Figures 7(c) and 7(f) show the calculation results. At different operating temperatures, the capacitive contribution increased with the scan rates. For the electrode operated at room temperature, at 0.1 mV·s^{-1}, the capacitive contribution is 59% and this value increases to 82% at 1 mV·s^{-1}. Notably, when operated under 60 °C at 0.1 mV·s^{-1}, the diffusion dominates the charge storage by contributing 64% of the current. With the increase of the scan rates, the ratio of the capacitive contribution gradually increases and at 1 mV·s^{-1}, it reaches 67%. As can be concluded from the above analysis, the P-CVO-HPs involve a pseudocapacitive charge storage mechanism. This might be originated from the porous nature of the electrode, which contributes increased surface area and thereby enhances charge transfer kinetics. While at the meantime, higher temperature is more favorable to boost the diffusion kinetics of ions in the electrolytes which results in improved rate and cycling performance of the electrodes.

4 Conclusions

In summary, porous $Co_2V_2O_7$ hexagonal prisms were synthesized successfully by a hydrothermal process followed with further combustion. The optimum amount of LiOH was determined via investigation over the morphological evolution and phase transition of the end products. As applied as anode for LIB cell, the P-CVO-HPs electrode exhibits a remarkable specific capacity (754 mAh·g^{-1} after 1,000 cycles at 5 A·g^{-1}), good long-term cyclability (206 mAh·g^{-1} after 6,000 cycles at 10 A·g^{-1}) and excellent rate performance. Even under extreme operating temperatures, the battery can still achieve stable cycling stability and rate capability (a capacity of 885 mAh·g^{-1} can be achieved when operating at 60 °C at 10 A·g^{-1} for 1,000 cycles). Finally, kinetics and quantitative calculation was carried out to better understand the pseudocapacitive-like electrochemical behavior and outstanding performance for lithium storage. It is expected that these P-CVO-HPs can be used as pseudocapacitive anode materials for next generation LIBs.

Acknowledgements

The authors gratefully acknowledge the National Natural Science Foundation of China (Nos. 21606003, 51802044, 51972067, 51672193, 51420105002, and 51920105004), and State Key Laboratory of Vanadium and Titanium Resources Comprehensive Utilization. The authors also acknowledge Singapore MOE AcRF Tier 2 under Grant Nos. 2018-T2-1-010 and MOE2017-T2-2-069, and National Research Foundation of Singapore (NRF) Investigatorship, award Number NRF2016NRF-NRFI001-22.

Electronic Supplementary Material: Supplementary material (fabrication procedure of P-CVO-HPs, characterization of hydrated CVO precursor (e.g., XRD patterns, SEM images, TGA, etc.), CV curves, discharge/charge curves, and a comparison table of the electrochemical performance) is available in the online version of this article at https://doi.org/10.1007/s12274-019-2547-9.

References

[1] Wang, Z. L.; Xu, D.; Wang, L. M.; Zhang, X. B. Facile and low-cost synthesis of large-area pure V_2O_5 nanosheets for high-capacity and high-rate lithium storage over a wide temperature range. *ChemPlusChem* **2012**, *77*, 124–128.

[2] Xu, G. J.; Huang, S. Q.; Cui, Z. L.; Du, X. F.; Wang, X.; Lu, D.; Shangguan, X. H.; Ma, J.; Han, P. X.; Zhou, X. H. et al. Functional additives assisted ester-carbonate electrolyte enables wide temperature operation of a high-voltage (5 V-Class) Li-ion battery. *J. Power Sources* **2019**, *416*, 29–36.

[3] Kafle, J.; Harris, J.; Chang, J.; Koshina, J.; Boone, D.; Qu, D. Y. Development of wide temperature electrolyte for graphite/LiNiMnCoO$_2$ Li-ion cells: High throughput screening. *J. Power Sources* **2018**, *392*, 60–68.

[4] Wang, J.; Nie, P.; Xu, G. Y.; Jiang, J. M.; Wu, Y. T.; Fu, R. R.; Dou, H.; Zhang, X. G. High-voltage $LiNi_{0.45}Cr_{0.1}Mn_{1.45}O_4$ cathode with superlong cycle performance for wide temperature lithium-ion batteries. *Adv. Funct. Mater.* **2018**, *28*, 1704808.

[5] Rodrigues, M. T. F.; Babu, G.; Gullapalli, H.; Kalaga, K.; Sayed, F. N.; Kato, K.; Joyner, J.; Ajayan, P. M. A materials perspective on Li-ion batteries at extreme temperatures. *Nat. Energy* **2017**, *2*, 17108.

[6] Lian, Q. W.; Zhou, G.; Liu, J. T.; Wu, C.; Wei, W. F.; Chen, L. B.; Li, C. C. Extrinsic pseudocapacitve Li-ion storage of SnS anode via lithiation-induced structural optimization on cycling. *J. Power Sources* **2017**, *366*, 1–8.

[7] Chen, D.; Tan, H. T.; Rui, X. H.; Zhang, Q.; Feng, Y. Z.; Geng, H. B.; Li, C. C.; Huang, S. M.; Yu, Y. Oxyvanite V_3O_5: A new intercalation-type anode for lithium-ion battery. *InfoMat* **2019**, *1*, 251–259.

[8] Li, H.; Peng, L.; Wu, D. B.; Wu, J.; Zhu, Y. J.; Hu, X. L. Ultrahigh-capacity and fire-resistant $LiFePO_4$-based composite cathodes for advanced lithium-ion batteries. *Adv. Energy Mater.* **2019**, *9*, 1802930.

[9] Tarascon, J. M.; Gozdz, A.; Schmutz, C.; Shokoohi, F.; Warren, P. Performance of Bellcore's plastic rechargeable Li-ion batteries. *Solid State Ionics* **1996**, *86*, 49–54.

[10] Aurbach, D.; Talyosef, Y.; Markovsky, B.; Markevich, E.; Zinigrad, E.; Asraf, L.; Gnanaraj, J. S.; Kim, H. J. Design of electrolyte solutions for Li and Li-ion batteries: A review. *Electrochim. Acta* **2004**, *50*, 247–254.

[11] Jiang, Y.; Liu, Z. Y.; Matsuhisa, N.; Qi, D. P.; Leow, W. R.; Yang, H.; Yu, J. C.; Chen, G.; Liu, Y. Q.; Wan, C. J. et al. Auxetic mechanical metamaterials to enhance sensitivity of stretchable strain sensors. *Adv. Mater.* **2018**, *30*, 1706589.

[12] Liu, F.; Chen, Z. X.; Fang, G. Z.; Wang, Z. Q.; Cai, Y. S.; Tang, B. Y.; Zhou, J.; Liang, S. Q. V_2O_5 nanospheres with mixed vanadium valences as high electrochemically active aqueous zinc-ion battery cathode. *Nano-Micro Lett.* **2019**, *11*, 25.

[13] Ji, W. X.; Wang, F.; Liu, D. T.; Qian, J. F.; Cao, Y. L.; Chen, Z. X.; Yang, H. X.; Ai, X. P. Building thermally stable Li-ion batteries using a temperature-responsive cathode. *J. Mater. Chem. A* **2016**, *4*, 11239–11246.

[14] Tang, B. Y.; Shan, L. T.; Liang, S. Q.; Zhou, J. Issues and opportunities facing aqueous zinc-ion batteries. *Energy Environ. Sci.* **2019**, in press, DOI: 10.1039/C9EE02526J.

[15] Yang, Y. Q.; Tang, Y.; Fang, G. Z.; Shan, L. T.; Guo, J. S.; Zhang, W. Y.; Wang, C.; Wang, L. B.; Zhou, J.; Liang, S. Q. Li^+ intercalated $V_2O_5{\cdot}nH_2O$ with enlarged layer spacing and fast ion diffusion as an aqueous zinc-ion battery cathode. *Energy Environ. Sci.* **2018**, *11*, 3157–3162.

[16] Zhang, S. S.; Xu, K.; Jow, T. R. A new approach toward improved low temperature performance of Li-ion battery. *Electrochem. Commun.* **2002**, *4*, 928–932.

[17] Qin, R. H.; Wei, Y. Q.; Zhai, T. Y.; Li, H. Q. LISICON structured $Li_3V_2(PO_4)_3$ with high rate and ultralong life for low-temperature lithium-ion batteries. *J. Mater. Chem. A* **2018**, *6*, 9737–9746.

[18] Liu, Y.; Yang, B. C.; Dong, X. L.; Wang, Y. G.; Xia, Y. Y. A simple prelithiation strategy to build a high-rate and long-life lithium-ion battery with improved low-temperature performance. *Angew. Chem., Int. Ed.* **2017**, *56*, 16606–16610.

[19] Chen, X. Z.; He, W. J.; Ding, L. X.; Wang, S. Q.; Wang, H. H. Enhancing interfacial contact in all solid state batteries with a

cathode-supported solid electrolyte membrane framework. *Energy Environ. Sci*. **2019**, *12*, 938–944.

[20] Jiang, Z. Y.; Xie, H. Q.; Wang, S. Q.; Song, X.; Yao, X.; Wang, H. H. Perovskite membranes with vertically aligned microchannels for all-solid-state lithium batteries. *Adv. Energy Mater*. **2018**, *8*, 1801433.

[21] Xiang, H. F.; Chen, J. J.; Li, Z.; Wang, H. H. An inorganic membrane as a separator for lithium-ion battery. *J. Power Sources* **2011**, *196*, 8651–8655.

[22] Yin, Z. G.; Qin, J. W.; Wang, W.; Cao, M. H. Rationally designed hollow precursor-derived $Zn_3V_2O_8$ nanocages as a high-performance anode material for lithium-ion batteries. *Nano Energy* **2017**, *31*, 367–376.

[23] Zhou, C. S.; Lu, J. M.; Hu, M. X.; Huang, Z. H.; Kang, F. Y.; Lv, R. T. High areal capacity Li-ion storage of binder-free metal vanadate/carbon hybrid anode by ion-exchange reaction. *Small* **2018**, *14*, 1801832.

[24] Lu, S. Y.; Zhu, T. X.; Li, Z. Y.; Pang, Y. C.; Shi, L.; Ding, S. J.; Gao, G. X. Ordered mesoporous carbon supported $Ni_3V_2O_8$ composites for lithium-ion batteries with long-term and high-rate performance. *J. Mater. Chem. A* **2018**, *6*, 7005–7013.

[25] Liu, P. C.; Zhu, K. J.; Gao, Y. F.; Luo, H. J.; Lu, L. Recent progress in the applications of vanadium-based oxides on energy storage: From low-dimensional nanomaterials synthesis to 3D micro/nano-structures and free-standing electrodes fabrication. *Adv. Energy Mater*. **2017**, *7*, 1700547.

[26] Li, M. L.; Gao, Y.; Chen, N.; Meng, X.; Wang, C. Z.; Zhang, Y. Q.; Zhang, D.; Wei, Y. J.; Du, F.; Chen, G. $Cu_3V_2O_8$ nanoparticles as intercalation-type anode material for lithium-ion batteries. *Chem.—Eur. J*. **2016**, *22*, 11405–11412.

[27] Zhang, X.; Yang, W. W.; Liu, J. G.; Zhou, Y.; Feng, S. C.; Yan, S. C.; Yao, Y. F.; Wang, G.; Wan, L.; Fang, C. et al. Ultralong metahewettite $CaV_6O_{16}\cdot 3H_2O$ nanoribbons as novel host materials for lithium storage: Towards high-rate and excellent long-term cyclability. *Nano Energy* **2016**, *22*, 38–47.

[28] Wang, J. L.; Pei, J.; Hua, K.; Chen, D. H.; Jiao, Y.; Hu, Y. Y.; Chen, G. Synthesis of $Co_2V_2O_7$ hollow cylinders with enhanced lithium storage properties using H_2O_2 as an etching agent. *ChemElectroChem* **2018**, *5*, 737–742.

[29] Chu, X. F.; Wang, H.; Chi, Y. D.; Wang, C.; Lei, L.; Zhang, W. T.; Yang, X. T. Hard-template-engaged formation of $Co_2V_2O_7$ hollow prisms for lithium ion batteries. *RSC Adv*. **2018**, *8*, 2072–2076.

[30] Wu, F. F.; Yu, C. H.; Liu, W. X.; Wang, T.; Feng, J. K.; Xiong, S. L. Large-scale synthesis of $Co_2V_2O_7$ hexagonal microplatelets under ambient conditions for highly reversible lithium storage. *J. Mater. Chem. A* **2015**, *3*, 16728–16736.

[31] Zhang, Q.; Pei, J.; Chen, G.; Bie, C. F.; Sun, J. X.; Liu, J. Porous $Co_3V_2O_8$ nanosheets with ultrahigh performance as anode materials for lithium ion batteries. *Adv. Mater. Interfaces* **2017**, *4*, 1700054.

[32] Wu, F. F.; Xiong, S. L.; Qian, Y. T.; Yu, S. H. Hydrothermal synthesis of unique hollow hexagonal prismatic pencils of $Co_3V_2O_8\cdot nH_2O$: A new anode material for lithium-ion batteries. *Angew. Chem., Int. Ed*. **2015**, *54*, 10787–10791.

[33] Luo, Y. Z.; Xu, X.; Zhang, Y. X.; Chen, C. Y.; Zhou, L.; Yan, M. Y.; Wei, Q. L.; Tian, X. C.; Mai, L. Q. Graphene oxide templated growth and superior lithium storage performance of novel hierarchical $Co_2V_2O_7$ nanosheets. *ACS Appl. Mater. Interfaces* **2016**, *8*, 2812–2818.

[34] Wang, Y. C.; Chai, H.; Dong, H.; Xu, J. Y.; Jia, D. Z.; Zhou, W. Y. Superior cycle stability performance of quasi-cuboidal CoV_2O_6 microstructures as electrode material for supercapacitors. *ACS Appl. Mater. Interfaces* **2016**, *8*, 27291–27297.

[35] Zhang, W. Y.; Fu, Y. S.; Liu, W. W.; Lim, L.; Wang, X.; Yu, A. P. A general approach for fabricating 3D MFe_2O_4 (M = Mn, Ni, Cu, Co)/graphitic carbon nitride covalently functionalized nitrogen-doped graphene nanocomposites as advanced anodes for lithium-ion batteries. *Nano Energy* **2019**, *57*, 48–56.

[36] Sambandam, B.; Soundharrajan, V.; Mathew, V.; Song, J. J.; Kim, S.; Jo, J.; Tung, D. P.; Kim, S.; Kim, J. Metal–organic framework-combustion: A new, cost-effective and one-pot technique to produce a porous $Co_3V_2O_8$ microsphere anode for high energy lithium ion batteries. *J. Mater. Chem. A* **2016**, *4*, 14605–14613.

[37] Soundharrajan, V.; Sambandam, B.; Song, J. J.; Kim, S.; Jo, J.; Kim, S.; Lee, S.; Mathew, V.; Kim, J. $Co_3V_2O_8$ sponge network morphology derived from metal–organic framework as an excellent lithium storage anode material. *ACS Appl. Mater. Interfaces* **2016**, *8*, 8546–8553.

[38] Jiang, T. C.; Bu, F. X.; Feng, X. X.; Shakir, I.; Hao, G. L.; Xu, Y. X. Porous Fe_2O_3 nanoframeworks encapsulated within three-dimensional graphene as high-performance flexible anode for lithium-ion battery. *ACS Nano* **2017**, *11*, 5140–5147.

[39] Yao, X.; Zhao, Y. L. Three-dimensional porous graphene networks and hybrids for lithium-ion batteries and supercapacitors. *Chem* **2017**, *2*, 171–200.

[40] Jung, H. G.; Jang, M. W.; Hassoun, J.; Sun, Y. K.; Scrosati, B. A high-rate long-life $Li_4Ti_5O_{12}/Li[Ni_{0.45}Co_{0.1}Mn_{1.45}]O_4$ lithium-ion battery. *Nat. Commun*. **2011**, *2*, 516.

[41] Chen, D.; Rui, X. H.; Zhang, Q.; Geng, H. B.; Gan, L. Y.; Zhang, W.; Li, C. C.; Huang, S. M.; Yu, Y. Persistent zinc-ion storage in mass-produced V_2O_5 architectures. *Nano Energy* **2019**, *60*, 171–178.

[42] Chao, D. L.; Xia, X. H.; Liu, J. L.; Fan, Z. X.; Ng, C. F.; Lin, J. Y.; Zhang, H.; Shen, Z. X.; Fan, H. J. A V_2O_5/conductive-polymer core/shell nanobelt array on three-dimensional graphite foam: A high-rate, ultrastable, and freestanding cathode for lithium-ion batteries. *Adv. Mater*. **2014**, *26*, 5794–5800.

[43] Yang, G. Z.; Cui, H.; Yang, G. W.; Wang, C. X. Self-Assembly of $Co_3V_2O_8$ multilayered nanosheets: Controllable synthesis, excellent Li-storage properties, and investigation of electrochemical mechanism. *ACS Nano* **2014**, *8*, 4474–4487.

[44] Lv, C. D.; Sun, J. X.; Chen, G.; Yan, C. S.; Chen, D. H. Achieving $Ni_3V_2O_8$ amorphous wire encapsulated in crystalline tube nano-structure as anode materials for lithium ion batteries. *Nano Energy* **2017**, *33*, 138–145.

[45] Zhu, C.; Liu, Z. Q.; Wang, J.; Pu, J.; Wu, W. L.; Zhou, Q. W.; Zhang, H. G. Novel Co_2VO_4 anodes using ultralight 3D metallic current collector and carbon sandwiched structures for high-performance Li-ion batteries. *Small* **2017**, *13*, 1701260.

[46] Zhang, L.; Zhao, K. N.; Luo, Y. Z.; Dong, Y. F.; Xu, W. W.; Yan, M. Y.; Ren, W. H.; Zhou, L.; Qu, L. B.; Mai, L. Q. Acetylene black induced heterogeneous growth of macroporous CoV_2O_6 nanosheet for high-rate pseudocapacitive lithium-ion battery anode. *ACS Appl. Mater. Interfaces* **2016**, *8*, 7139–7146.

[47] Ma, F. X.; Wu, H. B.; Xu, C. Y.; Zhen, L.; Lou, X. W. D. Self-organized sheaf-like Fe_3O_4/C hierarchical microrods with superior lithium storage properties. *Nanoscale* **2015**, *7*, 4411–4414.

[48] Zhang, D.; Li, G. S.; Li, B. Y.; Fan, J. M.; Liu, X. Q.; Chen, D. D.; Li, L. P. A facile strategy to fabricate V_2O_3/porous N-doped carbon nanosheet framework as high-performance anode for lithium-ion batteries. *J. Alloys Compd*. **2019**, *789*, 288–294.

[49] Feng, Y. H.; Chen, S. H.; Wang, J.; Lu, B. G. Carbon foam with microporous structure for high performance symmetric potassium dual-ion capacitor. *J. Energy Chem*. **2020**, *43*, 129–138.

[50] Wang, T.; Zhu, J.; Wei, Z. X.; Yang, H. G.; Ma, Z. L.; Ma, R. F.; Zhou, J.; Yang, Y. H.; Peng, L. L.; Fei, H. L. et al. Bacteria derived biological carbon building robust Li-S batteries. *Nano lett*. **2019**, *19*, 4384–4390.

[51] Wen, W.; Wu, J. M.; Jiang, Y. Z.; Lai, L. L.; Song, J. Pseudocapacitance-enhanced Li-ion microbatteries derived by a $TiN@TiO_2$ nanowire anode. *Chem* **2017**, *2*, 404–416.